PHYSICAL REVIEW C **85**, 024621 (2012)

Projectile fragmentation reactions of ^{40}Ar at 57 MeV/nucleon

X. H. Zhang (章学恒), Z. Y. Sun (孙志宇),* R. F. Chen (陈若富), Z. Q. Chen (陈志强), Z. Y. Guo (郭忠言),
J. L. Han (韩建龙), Z. G. Hu (胡正国), T. H. Huang (黄天衡), R. S. Mao (毛瑞士), Z. G. Xu (徐治国), M. Wang (王猛),
J. S. Wang (王建松), Y. Wang (王玥), G. Q. Xiao (肖国青), H. S. Xu (徐瑚珊), X. H. Yuan (袁小华), H. B. Zhang (张宏斌),
X. Y. Zhang (张雪荧), and T. C. Zhao (赵铁成)

Institute of Modern Physics, Chinese Academy of Sciences, Lanzhou 730000, China

(Received 26 September 2011; published 27 February 2012)

The projectile fragmentation reactions of ^{40}Ar at 57 MeV/nucleon on ^{9}Be and ^{181}Ta targets have been studied by the Radioactive Ion Beam Line in Lanzhou (RIBLL) at the Heavy-Ion Research Facility in Lanzhou (HIRFL). The momentum distributions of fragments have been measured and the competition between different mechanisms are observed. The production cross sections have been obtained and compared with the empirical parametrization of fragmentation cross section (EPAX), abrasion-ablation (AA), and heavy-ion phase space exploration (HIPSE) models, and the target dependence of fragment cross sections has also been discussed.

DOI: 10.1103/PhysRevC.85.024621 PACS number(s): 25.70.Mn, 27.30.+t

I. INTRODUCTION

The properties of isotopes far from the β stability valley have been one of the hot research fields in nuclear physics and astrophysics [1–3]. As an important tool for promoting this research, radioactive-ion-beam facilities based on projectile fragmentation have been established around the world [4–7], and the knowledge of reaction mechanisms of projectile fragmentation is very important for using these facilities effectively.

Since the pioneering work at Berkeley in 1970s [8,9], the reaction mechanism of projectile fragmentation (PF) has been studied extensively. For projectile-like fragments produced in the PF reactions at relativistic energies ($>$200 MeV/nucleon), the momentum distribution has been found to have a Gaussian shape [10] with its peak located around the velocity of the projectile [11] and whose width is well understood within the Goldhaber model [12]. The production cross sections can be estimated by the modified empirical parametrization of fragmentation cross sections (EPAX2) [13] and the abrasion-ablation (AA) model [14]. The "factorization" behavior, in which the cross sections are independent of projectile energy and vary only slowly with target mass [15,16], has been confirmed as a basic law of the PF reaction at relativistic energies.

However, at intermediate energies (20–200 MeV/nucleon), the momentum distribution of fragments has been found to have an asymmetric shape with a tail at the low-momentum side [17]. The experiments using primary beams of ^{40,48}Ca and ^{58,64}Ni at 140 MeV/nucleon on ^{9}Be and ^{181}Ta targets have showed that the cross sections are overestimated in EPAX2 calculations for the fragments far from the stability valley [18]. Similar results have been found in experiments of ^{86}Kr at 64 MeV/nucleon and ^{40}Ar at 90–94 MeV/nucleon on ^{9}Be and ^{181}Ta targets [19,20]. In addition, experiments have also shown that the production cross sections of the isotopes far from the stability valley are enhanced in the reactions on ^{181}Ta target, which implies that the factorization hypothesis is invalid for very neutron-rich and very proton-rich isotopes, maybe due to the transfer reaction involved [20,21].

In this paper, we would like to report the results from the reactions of a 57 MeV/nucleon ^{40}Ar beam on ^{9}Be and ^{181}Ta targets.

II. EXPERIMENT

The experiment was performed at the Heavy-Ion Research Facility in Lanzhou (HIRFL) [22,23]. The whole experimental setup is shown schematically in Fig. 1. A primary beam of 57 MeV/nucleon ^{40}Ar was extracted from the Separate Sector Cyclotron (SSC) and implanted into the production targets at the entrance of the Radioactive Ion Beam Line in Lanzhou (RIBLL) [24], which is a double achromatic antisymmetry spectrometer. The products were transported to the final focal point F4 through RIBLL and the secondary part of the RIBLL served as a zero-degree spectrometer.

The intensity of the primary beam was measured by a thin secondary-electron emitter, which is similar to the Secondary electron transmission monitor (SEETRAM) detector at the GSI FRagment Separator (FRS) [7,25], and was placed at the upstream of the production target and calibrated by a Faraday cup over the range of 5–20 enA. Two targets, ^{9}Be and ^{181}Ta, with thicknesses of 94 and 95 mg/cm^2, respectively, were used in the experiment.

Particle identification was performed by combining the time of flight (ToF), the energy deposit ΔE, the total energy E, and the magnetic rigidity $B\rho$; this method is widely used by all PF-type separators. The ToF was measured by using two 50-μm-thick plastic scintillation detectors installed at the points F2 and F4 with a flight path of 17 m, and a time resolution of 300 ps (full width at half maximum, FWHM) was obtained for the whole system [26]. The ΔE and E information were obtained by using a telescope placed at F4, which consisted of two 325-μm-thick 45 × 45 mm^2 silicon detectors followed by a 1-cm-thick CsI(Tl) crystal. The $B\rho$ value was determined from the magnetic setting of RIBLL. In addition, three position-sensitive parallel plate avalanche counters (PPAC) placed at F2, F3, and F4 were used to monitor the position of the fragments.

---

[*] sunzhy@impcas.ac.cn

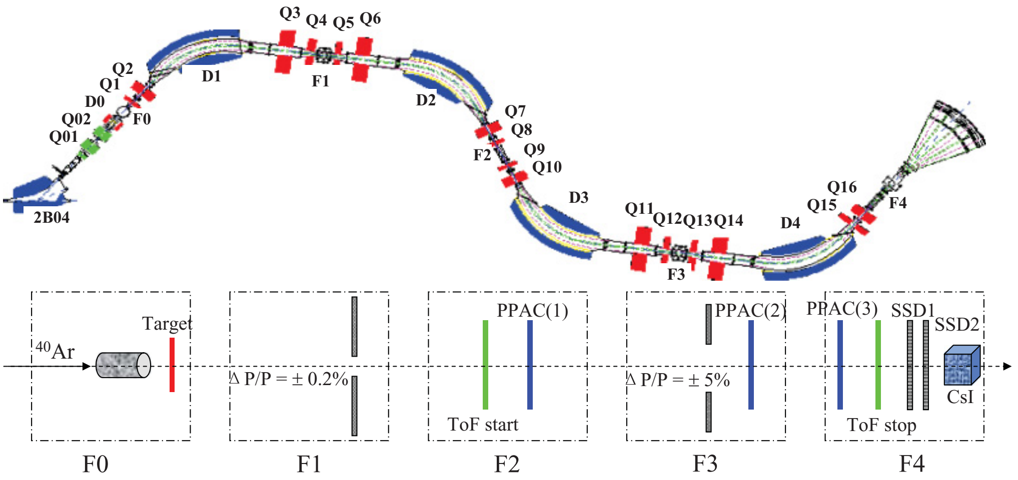

FIG. 1. (Color online) Layout of RIBLL and experimental setup.

To simplify the transmission calculation, the momentum acceptance of RIBLL, $\Delta p/p$, was limited to $\pm 0.2\%$ by a set of slits located at the first focal plane F1 in the experiment, thus the products could only travel close to the optical axis of the separator. The momentum distributions of the fragments were measured by scanning the magnetic rigidity settings of the separator over a range of 1.65–2.7 Tm in 33 steps for the ^{9}Be target and 1.76–2.7 Tm in 25 steps for the ^{181}Ta target.

III. DATA ANALYSIS

A typical ΔE-ToF spectrum for the $^{40}\mathrm{Ar} + {}^{9}\mathrm{Be}$ reaction at $B\rho = 2.5$ Tm is shown in Fig. 2(a). It is easy to calculate the mass number A_f and charge number Z_f for each fragment by taking into account the corresponding $B\rho$, ToF, and ΔE information. Figure 2(b) shows the corresponding plot of Z_f versus the neutron excess $N_\mathrm{f} - Z_\mathrm{f}$, where the neutron number $N_\mathrm{f} = A_\mathrm{f} - Z_\mathrm{f}$. It can be seen that the particle identification is very clear. The root-mean-square (rms) widths of Z_f and $N_\mathrm{f} - Z_\mathrm{f}$ were determined to be less than 0.13 and 0.10, respectively.

After interaction with materials, the fragments may have various charge states other than fully stripped; their losses in the separator are due to the changed magnetic rigidities. In our experiment, we saw clear evidence of both fully stripped and hydrogen-like particles in the ΔE-E spectra. The contributions of hydrogen-like particles were determined to be less than 1.0% and 2.9% for the $^{40}\mathrm{Ar} + {}^{9}\mathrm{Be}$ and $^{40}\mathrm{Ar} + {}^{181}\mathrm{Ta}$ reactions, respectively.

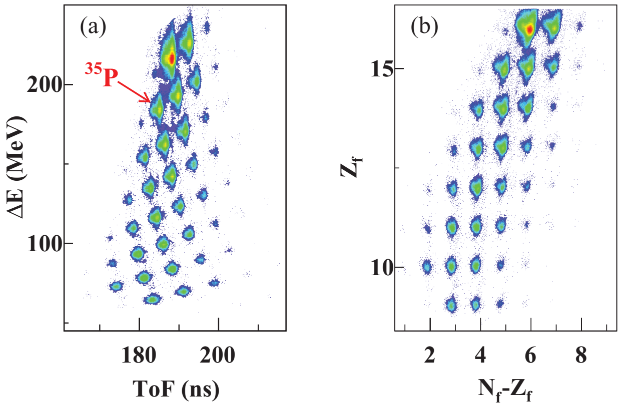

FIG. 2. (Color online) Particle identification spectra for the $^{40}\mathrm{Ar} + {}^{9}\mathrm{Be}$ reaction at $B\rho = 2.5$ Tm.

The differential cross section $d\sigma/dp$ can be calculated from

$$\frac{d\sigma}{dp} = \frac{N(A_\mathrm{f}, Z_\mathrm{f})}{kN_B N_S \Delta p}\frac{1}{\varepsilon}, \tag{1}$$

where $N(A_\mathrm{f}, Z_\mathrm{f})$ is the number of fragments with A_f and Z_f, which was extracted by integration over an area of $\pm 2\sigma$ (95% confidence level) in the Z_f vs $N_\mathrm{f} - Z_\mathrm{f}$ spectrum, N_B and N_S are the number of beam particles and target nuclei, respectively, Δp is the momentum acceptance of the separator, ε is the transmission efficiency, and k is a correction factor which includes all the other effects, such as the efficiency of the detectors, the dead time of the data acquisition, and so on.

The code LISE++ [27] was used to simulate the transmission processes. In the simulations, the emittance of 5π mm mrad in both horizontal and vertical directions was used for the primary beam. The transmission efficiency $\varepsilon = N_{\mathrm{F4}}/N_{\mathrm{F0}}$, where N_{F4} and N_{F0} are the number of particles transported to the focal point F4 of RIBLL and that measured at the target point F0, respectively. To obtain N_{F0}, the longitudinal momentum distribution of the fragments was obtained from a universal parametrization model [28] and the transverse momentum distribution was calculated from a Gaussian function with variance $\sigma_\perp$ [29]:

$$\sigma_\perp^2 = \sigma_0^2 \frac{A_\mathrm{f}(A_\mathrm{p} - A_\mathrm{f})}{A_\mathrm{p} - 1} + \sigma_D^2 \frac{A_\mathrm{f}(A_\mathrm{f} - 1)}{A_\mathrm{p}(A_\mathrm{p} - 1)}, \tag{2}$$

where A_p is the mass number of the projectile, σ_0 is the usual term due to the intrinsic nucleon motion, and σ_D is the orbital dispersion. The first term of Eq. (2) comes from the Goldhaber model, and the second term takes into account the deflection of the projectile by the target nucleus, which is significant only at low and intermediate energies. In our simulations, the values of 90 and 200 MeV$/c$ were used for σ_0 and σ_D, respectively. The angular distribution of fragments can be calculated from their

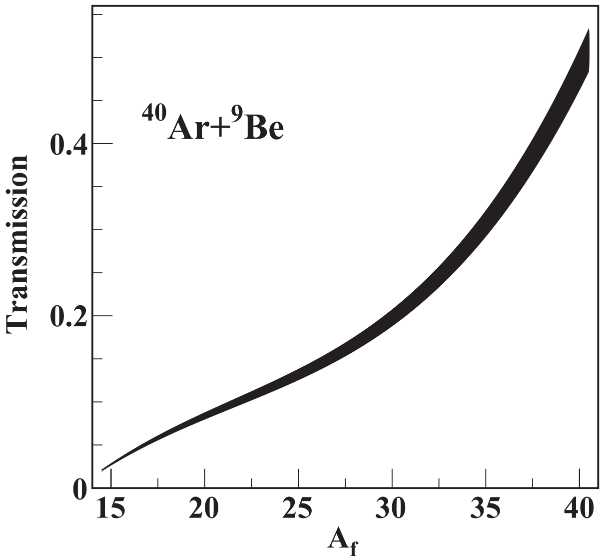

FIG. 3. Transmission efficiency as a function of fragment mass number for the ^{40}Ar+^{9}Be reaction.

longitudinal and transverse momentums, and it will be much broader for light fragments. Because the angular acceptance of RIBLL is only 50 mrad both in horizontal and vertical directions, the transmission efficiency ε is mass dependant. Figure 3 shows the transmission efficiency as a function of A_f for the $^{40}\mathrm{Ar} + {}^{9}\mathrm{Be}$ reaction, in which the shaded region is the uncertainty estimated from the simulations. The uncertainty is less than 10% and is dominated mainly by the uncertainties of the primary beam emittance and the transverse momentum distribution of the fragments.

The momentum distribution of a fragment can be fit with an asymmetric Gaussian function,

$$\frac{d\sigma}{dp} = \begin{cases} s \exp\left[-(p-p_0)^2/\left(2\sigma_L^2\right)\right] & (p \leqslant p_0) \\ s \exp\left[-(p-p_0)^2/\left(2\sigma_R^2\right)\right] & (p > p_0), \end{cases} \tag{3}$$

where s is the normalization factor, p_0 is the peak position, σ_L and σ_R are the widths for the left and right sides of the distribution, respectively. For the fragments with fully measured momentum distribution, these parameters were obtained by the least-squares method. Figure 4(a) shows the momentum distribution of ^{33}P produced at the $^{40}\mathrm{Ar} + {}^{9}\mathrm{Be}$ reaction, where the solid curve is the best fit to Eq. (3). For the fragments with only partly measured momentum distributions, we used the systematic values of p_0, σ_L and σ_R, obtained from the systematic behaviors of the fragments with fully measured momentum distributions. Figure 4(b) shows the momentum distribution of ^{32}Cl at the $^{40}\mathrm{Ar} + {}^{9}\mathrm{Be}$ reaction, where the solid curve is the calculated momentum distribution.

The production cross section of one fragment was obtained by integrating its momentum distribution. The error was estimated to be less than 14%, which included the contributions mainly from the uncertainties of the statistics, the primary beam intensity, the transmission, and the extrapolation of the parameters (for the fragments with only partly measured momentum distributions).

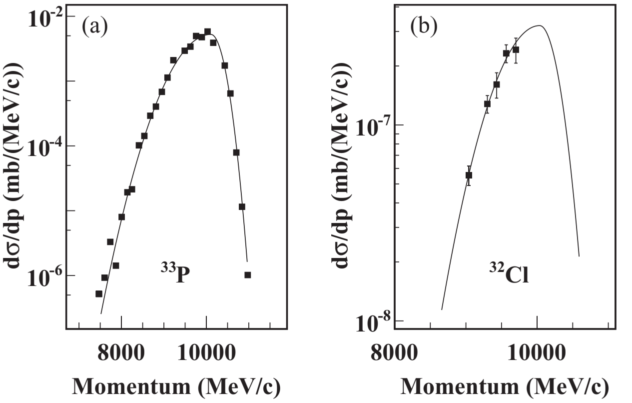

FIG. 4. Fragment momentum distributions of ^{33}P (a) and ^{32}Cl (b) produced in the $^{40}\mathrm{Ar} + {}^{9}\mathrm{Be}$ reaction. The solid curves are the fit results by using Eq. (3).

IV. RESULTS AND DISCUSSION

A. Momentum distributions

The momentum distributions of projectile-like fragments provide valuable information about the reaction mechanism. To study this, only the isotopes with fully measured momentum distributions have been used in the analysis.

In the nuclear fragmentation process, the velocity of the fragment is smaller than that of the projectile, for part of the projectile kinetic energy has been converted into excitation energy of the fragment. This energy loss is called "momentum peak shift," and can be seen clearly from the difference of the velocity of the projectile and the most probable velocities of the fragments, which is shown in Fig. 5 for the $^{40}\mathrm{Ar} + {}^{9}\mathrm{Be}$ and $^{40}\mathrm{Ar} + {}^{181}\mathrm{Ta}$ reactions. In order eliminate the influence of the target thickness, all data have been corrected to the values at the center of the targets and normalized by the velocities of the projectile at that point (which correspond to 53.56 MeV/nucleon in the Be target and 54.93 MeV/nucleon in the Ta target). The solid curves are the predictions of the Borrel model, which suggests that the momentum peak shift can be simply explained by the amount of binding energy (8 MeV/nucleon in average) of the removed nucleons will be subtracted from the kinetic energy of the remaining part of the projectile. In our experimental results, the most probable

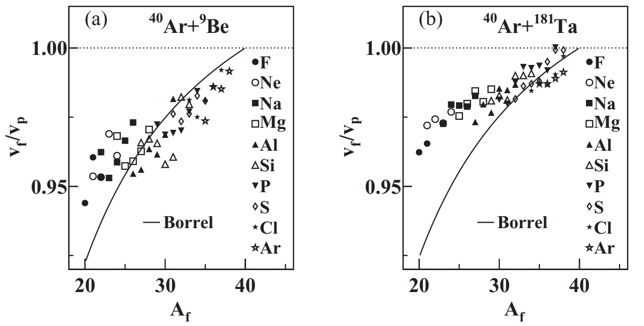

FIG. 5. Momentum peak shifts of fragments produced in the $^{40}\mathrm{Ar} + {}^{9}\mathrm{Be}$ (a) and $^{40}\mathrm{Ar} + {}^{181}\mathrm{Ta}$ (b) reactions. The solid curves are the predictions of Borrel model.

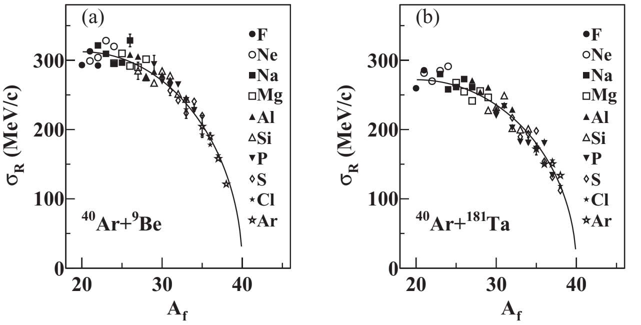

FIG. 6. High-momentum-side widths of fragments produced in $^{40}\text{Ar} + {}^{9}\text{Be}$ (a) and $^{40}\text{Ar} + {}^{181}\text{Ta}$ (b) reactions. The solid curves are the fit results by the Goldhaber model.

velocities can be roughly reproduced by the Borrel model for the fragments close to the projectile. But for the fragments with $A_f \leqslant 30$, the most probable velocities are always much larger than the ones expected in the Borrel model. This dispersion implies that the production of light fragments is dominated by another mechanism, which costs less energy than the removal of free individual nucleons. We think the possible explanation could be the multifragmentation process, in which the projectile will be split into two (or even more) massive pieces.

Figure 6 shows the high-momentum-side width, σ_R, as a function of A_f for both reaction systems. The solid curves represent the fits with the Goldhaber model, and the values σ_0 of 92.7 ± 4.2 and 85.4 ± 5.1 MeV/c are obtained for the $^{40}\text{Ar} + {}^{9}\text{Be}$ and $^{40}\text{Ar} + {}^{181}\text{Ta}$ reactions, respectively. The results are in good agreement with the suggested value of 90 MeV/c obtained in the relativistic energies [30–32]. This indicates that the production of high momentum fragments are dominated by "pure" projectile fragmentation reaction, which has no nucleon transfer in the abrasion stage.

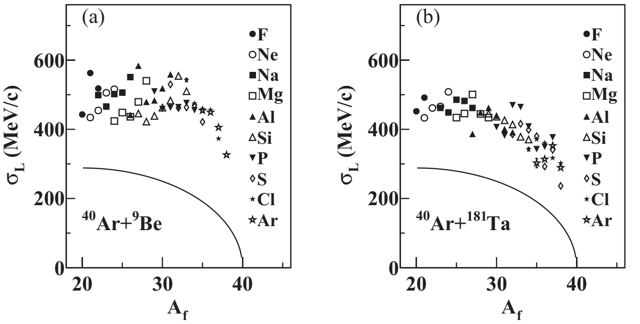

FIG. 7. Low-momentum-side widths of fragments produced in $^{40}\text{Ar} + {}^{9}\text{Be}$ (a) and $^{40}\text{Ar} + {}^{181}\text{Ta}$ (b) reactions. The solid curves are predictions by the Goldhaber model with $\sigma_0 = 90$ MeV/c.

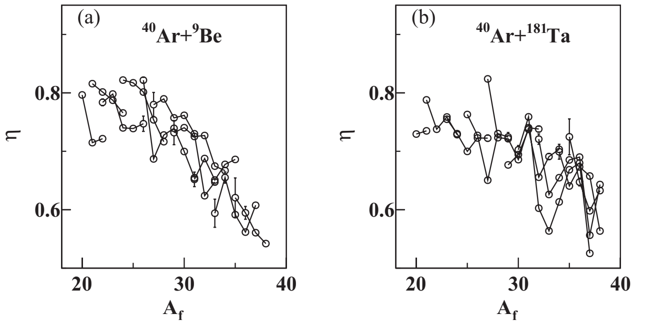

FIG. 8. Contributions of "pure" fragmentation reaction to the total production cross sections for $^{40}\text{Ar} + {}^{9}\text{Be}$ (a) and $^{40}\text{Ar} + {}^{181}\text{Ta}$ (b) reactions. The black lines connecting the isotope chains are only to guide the eye.

Figure 7 shows the low-momentum-side width, σ_L. The solid curves are the predictions of Goldhaber model with $\sigma_0 = 90$ MeV/c. It is very clear that the experimental data are much larger than the model predictions. This broader distribution indicates that some processes must exist in the reaction to cause a large energy loss. Earlier works [28,33,34] suggested that this large energy loss is mainly due to the nucleon transfer process between projectile and target nuclei in the abrasion stage. Assuming that the contribution of the "pure" fragmentation process has a symmetric Gaussian-shaped momentum distribution with width σ_R, we can calculate the ratios of "pure" fragmentation reaction contributed to the total production cross sections as

$$\eta = 2\sigma_R/(\sigma_L + \sigma_R). \tag{4}$$

The obtained ratio η is shown in Fig. 8. For the fragments close to the projectile, the "pure" fragmentation process contributes only 50%–60% of the products, which implies a very large possibility for nucleon transfer in the abrasion stage. The η value increases with decreasing mass of the fragment, and up to 80% for the fragments with masses around half of the projectile. In the AA model, the light fragments are produced in reactions with large overlap between the projectile and the target nuclei. Because the possibility of nucleon transfer is proportional to the number of nucleons within the overlap region, this picture is not in agreement with our results for the light fragments; that is, larger η means smaller overlap. We think this may be more evidence for the existence of the multifragmentation process.

B. Cross sections

Figure 9 shows the experimental production cross-sections of about 100 isotopes with $Z_f \geqslant 9$ obtained from the $^{40}\text{Ar} + {}^{9}\text{Be}$ and $^{40}\text{Ar} + {}^{181}\text{Ta}$ reactions. For comparison, we used three

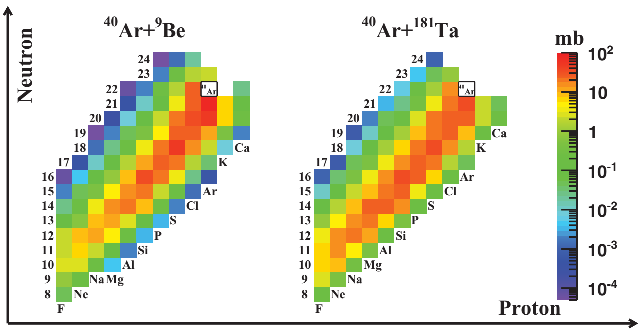

FIG. 9. (Color online) Production cross sections of projectile-like fragments for ^{40}Ar at 57 MeV/nucleon on the ^{9}Be and ^{181}Ta targets.

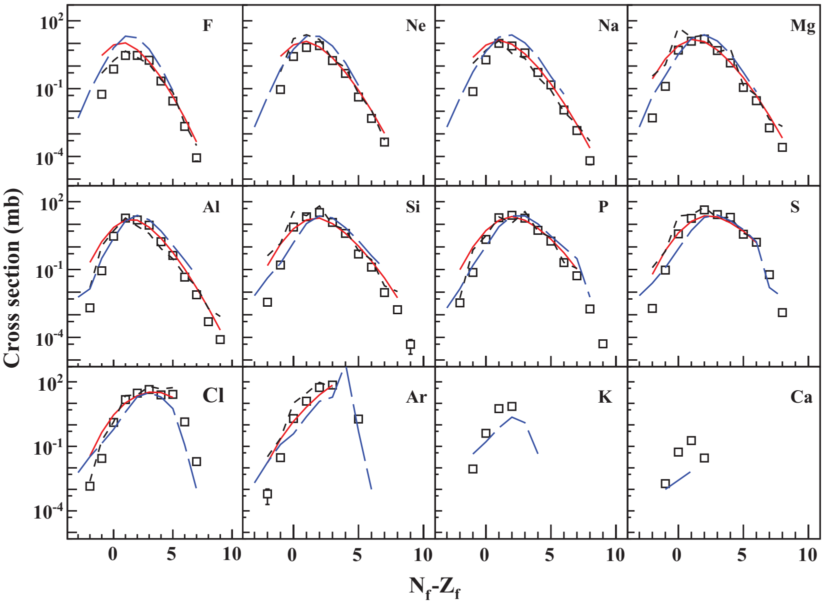

FIG. 10. (Color online) Production cross sections for fragments in the ^{40}Ar + ^{9}Be reaction. Open squares show the experimental data, and solid, dashed, and long dashed lines show the calculations by the EPAX, AA, and HIPSE models, respectively.

different models: empirical parametrization of fragmentation cross sections (EPAX) [13], AA [14], and heavy-ion phase space exploration (HIPSE) [35], to estimate the production cross-sections of projectile fragments. The results from the calculations are also shown in Fig. 10 for the ^{40}Ar + ^{9}Be system and in Fig. 11 for the ^{40}Ar + ^{181}Ta system.

Although the parametrized formula EPAX2 was derived from the data of target spallation and projectile fragmentation reactions at relativistic energies, we can still use it to estimate the production cross sections in our experiments due to the "factorization." After a detailed comparison with our experimental data, we think that the EPAX2 formula can well estimate the cross sections for the fragments near the stability line, but for the ones far from the stability line, especially in the proton-rich side, the cross sections are over estimated by the formula.

In the AA model, the prefragment cross section is determined by the fireball scheme; that is, the proton-to-neutron ratio of the prefragment is the same as that of the projectile [36], and the excitation energy of the prefragment is proportional to the number of removed nucleons from the projectile. The code included in the LISE++ [37] was used for our calculation. In our calculation, the value of 13.3 MeV/nucleon, estimated by the particle-hole pair model [38], was used for the excitation energy of the prefragment, and the deexcitation of the prefragments was treated by the analytical LISFUS evaporation code [39]. After comparing with our data, we think that the AA model can reproduce the experimental data better than the EPAX2 calculations, especially for the neutron-rich and proton-rich fragments.

As mentioned above in the previous section, the nucleon transfer process in the abrasion stage plays an important role

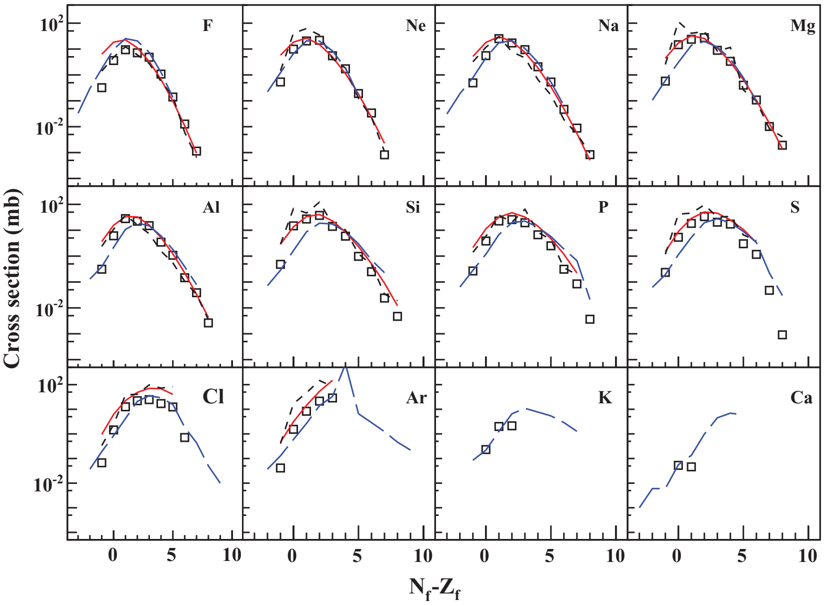

FIG. 11. (Color online) Production cross section for fragments in the ^{40}Ar + ^{181}Ta reaction. The same conventions as in Fig. 10 are used.

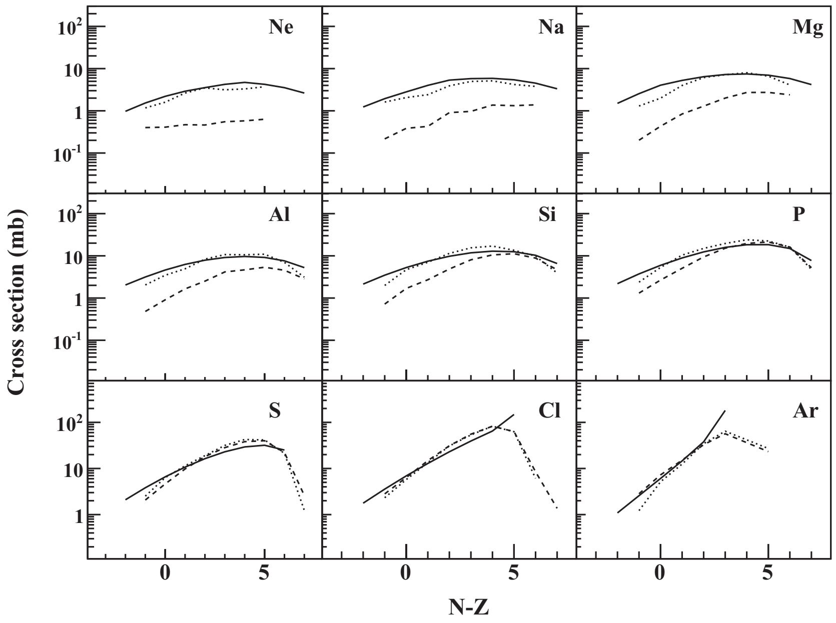

FIG. 12. Isotope distribution of prefragments as a function of neutron excess of fragments in 57 MeV/nucleon ^{40}Ar + ^{9}Be reaction. The solid, dashed, and dotted lines show the calculations by AA model, HIPSE model with nucleon transfer process, and HIPSE model without nucleon transfer process, respectively.

in the reactions. This process is not considered in the AA model. To study this, we did calculations with the HIPSE model [35], which describes both dynamical and statistical aspects of nuclear collisions in the intermediate-energy range of 30–150 MeV/nucleon.

There are three important parameters in the HIPSE model: the hardness of the potential, α_a, the percentage of nucleons transferred between the projectile and target, χ_{ex}, and the percentage of nucleon-nucleon collisions in the overlap region, χ_{coll}. Based on the values adjusted for beam energies of 10, 25, 50, and 80 MeV/nucleon [40], the values of $\alpha_a = 0.206$, $\chi_{\text{ex}} = 0.294$, and $\chi_{\text{coll}} = 0.056$ for the ^{40}Ar + ^{9}Be reaction and $\alpha_a = 0.208$, $\chi_{\text{ex}} = 0.292$, and $\chi_{\text{coll}} = 0.058$ for the ^{40}Ar + ^{181}Ta reaction were extrapolated and used in our calculation. The deexcitation of prefragments was achieved by the SIMON code [41]. In order to compare with our experimental data, all isotopic distributions were normalized by the estimated total cross section.

The isotope distributions of prefragments calculated by the AA and HIPSE models are shown in Fig. 12 for the ^{40}Ar + ^{9}Be reaction. For the prefragments with charge number Z_f, the isotope distribution calculated by the HIPSE model is narrower than that obtained by the AA model, and this difference becomes larger while the number of nucleons removed from the projectile increases. This difference is mainly due to the transfer process in the HIPSE model because, if we turn off this process in the calculation, the results, which are plotted as dotted lines in Fig. 12, are nearly same as those from the AA model.

The calculated mean excitation energies of prefragments are shown in Fig. 13. The shaded regions depict fluctuations expressed in terms of one standard deviation around the mean in HIPSE calculations. We can see that the mean excitation energy calculated by the AA model increases monotonically

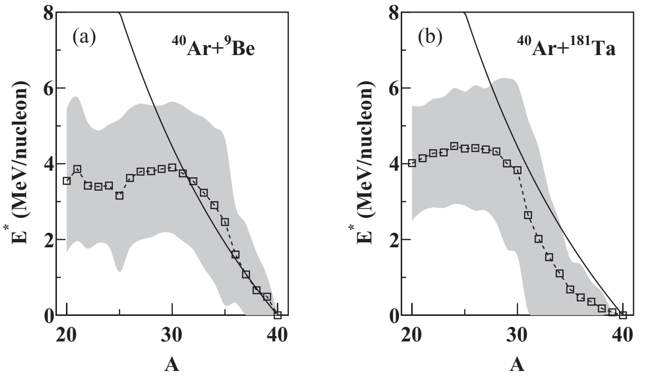

FIG. 13. Excitation energy, calculated by AA model (solid line) and HIPSE model (open squares), plotted as a function of prefragment mass number for the ^{40}Ar + ^{9}Be (a) and ^{40}Ar + ^{181}Ta (b) reactions. The shaded regions depict fluctuations expressed in terms of one standard deviation around the mean in HIPSE calculations.

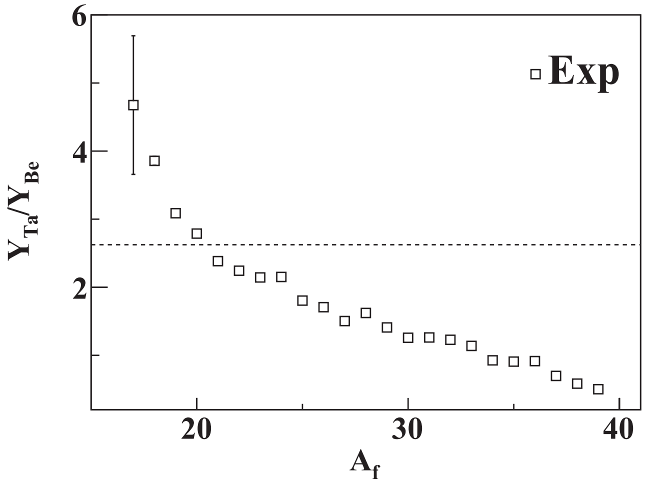

FIG. 14. Ratios of mass yields between ^{40}Ar + ^{181}Ta and ^{40}Ar + ^{9}Be reactions. The solid line represents the results calculated with Eq. (5).

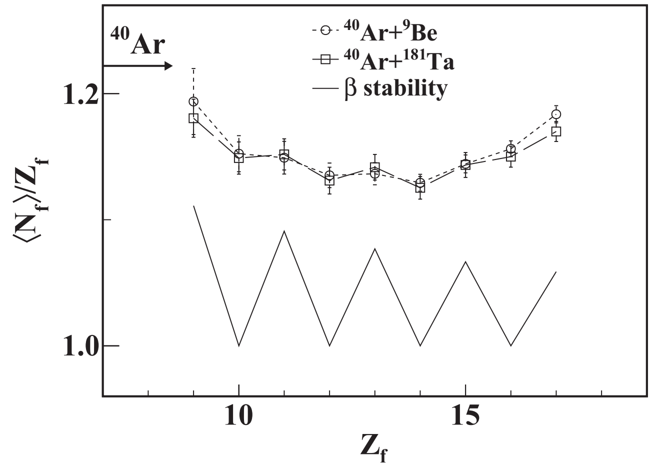

FIG. 15. Mean N_f/Z_f ratio for $^{40}\text{Ar} + {}^{9}\text{Be}$ (open circles) and $^{40}\text{Ar} + {}^{181}\text{Ta}$ (open squares) reactions. The solid line depicts the β stability line, and the arrow represents N/Z for the ^{40}Ar projectile.

upon removing nucleons from the projectile. But in the HIPSE model, the excitation energy has a rapid rise at beginning, and saturates quickly around 4 MeV/nucleon after removing about 10 nucleons from the projectile. This excitation energy saturation is consistent with the momentum-peak-shift results in Fig. 5.

The prefragments with high excitation energy will deexcite by evaporating light particles. If we assume that the evaporated nucleons are emitted homogeneously from the prefragments, the mean velocity of the final fragments will be the same as that of the prefragments. According to conservation of energy, the velocity difference between projectile and fragment is proportional to the excitation energy of the prefragment. From Fig. 5, it can be seen that the velocity differences in the $^{40}\text{Ar} + {}^{9}\text{Be}$ reaction are larger than those in the $^{40}\text{Ar} + {}^{181}\text{Ta}$ reaction, which is similar to the HIPSE calculations, especially for those with $A_f \geqslant 30$.

C. Target dependence

In the reactions at relativistic energies, the target dependence on cross section is only due to the target-size effect; the so-called factorization. But at intermediate energies, different results have already been observed by many groups [19–21,42].

Let us define $Y(A_f)$ as the total cross section for all the fragments with the same A_f. According to the factorization, the ratio of yields $Y(A_f)$ between the $^{40}\text{Ar} + {}^{181}\text{Ta}$ and $^{40}\text{Ar} + {}^{9}\text{Be}$ reactions can be described as

$$\frac{Y_{\text{Ta}}}{Y_{\text{Be}}} = \frac{\left(A_p^{1/3} + A_{\text{Ta}}^{1/3}\right)^2}{\left(A_p^{1/3} + A_{\text{Be}}^{1/3}\right)^2}, \tag{5}$$

where A_p, A_{Be}, and A_{Ta} are the mass number of the projectile, ^{9}Be, and ^{181}Ta targets, respectively. For our case, this ratio equals 2.72. Obviously, it is not in agreement with our experimental data, which are shown in Fig. 14. In our experiment, the ratio decreases with increasing mass number of the fragments.

From isotope distributions, we can get the mean neutron number for each Z_f from

$$\langle N_f\rangle = \frac{\sum_i N_i\sigma_i}{\sum_i \sigma_i}, \tag{6}$$

where N_i and σ_i are the neutron number and corresponding cross section, respectively. The $\langle N_f\rangle/Z_f$ ratio for ^{9}Be and ^{181}Ta targets are shown in Fig. 15. A clear memory effect can be observed for the fragments close to the projectile, for they try to keep the same isospin. When more nucleons are removed, effects such as nucleon transfer and evaporation tend to lead the isospin close to the β stability line. The interesting thing is that, for the light fragments, the $\langle N_f\rangle/Z_f$ ratio goes toward the projectile again, which is different from some early works [43–46]. Although the N/Z values of ^{9}Be and ^{181}Ta are much different (1.25 for ^{9}Be and 1.479 for ^{181}Ta), no obvious difference has been observed for the $\langle N_f\rangle/Z_f$ ratio.

The ratios of the fragment cross sections between the $^{40}\text{Ar} + {}^{181}\text{Ta}$ reaction and the $^{40}\text{Ar} + {}^{9}\text{Be}$ reaction are shown as a function of $Z_\beta - Z_f$ in Fig. 16(a). Here Z_f is the proton number of the fragment, and Z_β is the proton number corresponding to the β stability line for a given mass number A_f, which can be calculated by $Z_\beta = A_f/(1.98 + 0.0155A_f^{2/3})$. To eliminate the target-size effect, the fragment cross section is normalized by the experimental mass yield $Y(A_f)$. Obviously, the ratios have a U-shaped distribution for each isobar, which means that the production cross sections of neutron-rich ($Z_\beta - Z_f > 1$) and proton-rich ($Z_\beta - Z_f < -1$) isotopes are enhanced in the $^{40}\text{Ar} + {}^{181}\text{Ta}$ reaction.

We think the enhancement for proton-rich fragments is mostly due to the deexcitation process. The deexcitation of prefragments by evaporating light particles will make the residues move toward the β stability line. According to Fig. 13, the prefragments produced in the $^{40}\text{Ar} + {}^{181}\text{Ta}$ reaction have less excitation energy than those in the $^{40}\text{Ar} + {}^{9}\text{Be}$ reaction, which means that they will evaporate less nucleons and more easily keep their original isospins. Figure 17 shows the same

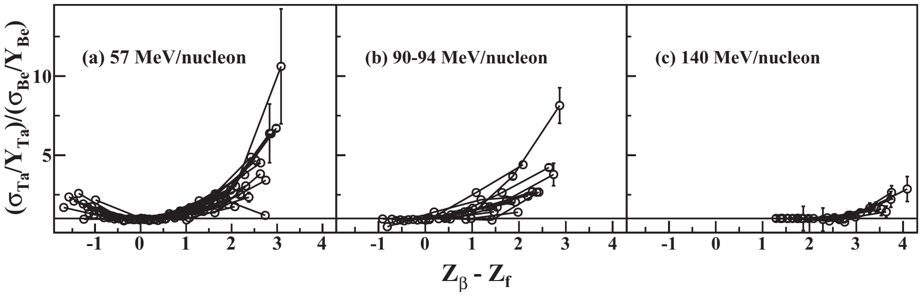

FIG. 16. Ratios of production cross sections between $^{40}\text{Ar} + {}^{181}\text{Ta}$ and $^{40}\text{Ar} + {}^{9}\text{Be}$ reactions at (a) 57 MeV/nucleon, (b) 90–94 MeV/nucleon, and (c) 140 MeV/nucleon. The lines connecting the isobars are only to guide the eye.

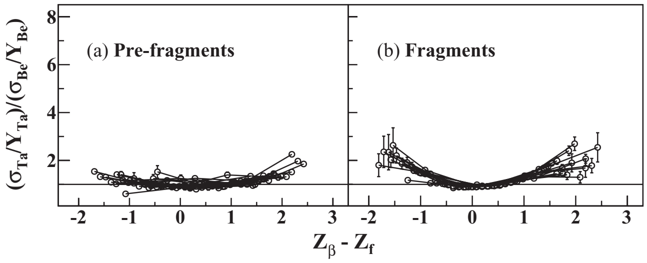

FIG. 17. Cross-section ratios between ^{40}Ar + ^{181}Ta and ^{40}Ar + ^{9}Be reactions at 57 MeV/nucleon calculated by HIPSE model. The lines connecting the isobars are only to guide the eye.

ratios calculated by HIPSE model for prefragments and their evaporation residues. We can see that there is no obvious difference for the prefragments, but there is an enhancement in proton-rich side for the residues.

For the neutron-rich side, the enhancement is more obvious, which cannot be explained only with the deexcitation process. Many mechanisms may contribute to this enhancement, such as the nucleon transfer in the abrasion stage and the isospin dependence of nucleon-nucleon interaction.

The significance of nucleon transfer in this energy regime can be proven by the observed isotopes of ^{37}Si, ^{38,39}P, ^{39,40}S, ^{40,41}Cl, ^{41}Ar, $^{37–40}$K, and $^{39–42}$Ca, which have more neutrons or protons than the projectile. Since ^{181}Ta is more neutron rich than ^{9}Be, the probability of neutron transfer should be larger, leading to more neutron-rich prefragments.

As is well known, the proton-to-neutron scattering cross section (σ_{np}) is larger than those for proton to proton (σ_{pp}) and neutron to neutron (σ_{nn}) when the nucleon energy is less than 500 MeV. This difference may lead to the deviation of prefragment charge distributions, which means the neutron-rich target nucleus easily knocks out protons in the projectile nucleus in the abrasion stage, and the production of neutron-rich prefragments is promoted.

Because the contributions of both mechanisms are energy dependent, we can verify which one is dominate via observing the variation of cross-section ratios with varying projectile energy. For comparison, the cross-section ratios of 90–94 MeV/nucleon and 140 MeV/nucleon ^{40}Ar on ^{9}Be and ^{181}Ta targets [20,42] are also shown in Fig. 16. For the neutron-rich fragments, it can be seen that the cross-section ratios decrease rapidly with increasing projectile energy. Because the ratios σ_{np}/σ_{pp} or σ_{np}/σ_{nn} only change by about 20% from 50 to 140 MeV/nucleon [47], which is too small for the observed changes, we think the enhancement of neutron-rich fragments in the ^{40}Ar + ^{181}Ta reaction may due to the nucleon-transfer process in the abrasion stage, which decreases rapidly with increasing projectile energy and finally becomes negligible at relativistic energies.

However, the discussions so far are still qualitative, and more experiments at different energies are needed to further examine and elucidate this hypothesis.

V. SUMMARY

The projectile fragmentation reactions of a 57 MeV/nucleon ^{40}Ar beam on ^{9}Be and ^{181}Ta targets have been studied by RIBLL at the HIRFL.

By measuring the momentum distribution of the fragments, we have seen clearly the competition between projectile fragmentation and other mechanisms in the production of fragments. The high-momentum-side widths of the fragments are in good agreement with the Goldhaber model, which shows that the projectile fragmentation reaction is dominant. The low-momentum-side widths are much broader, which may come from the nucleon transfer between the projectile and target nuclei during the reaction process. For the fragments close to the projectile, the contribution from the nucleon transfer process is nearly the same as the projectile fragmentation process but, for light fragments, the production is dominated by the multifragmentation process.

The production cross sections of the fragments have been studied with the HIPSE model. The calculations show that the nucleon transfer process in the abrasion stage has an important influence on the isotope distributions of prefragments, and the calculated excitation energies of the prefragments can explain well the measured momentum-peak shifts.

The target dependance of the production cross sections has also been studied. The factorization assumption is not correct for this low beam energy. Compared to the ^{9}Be target, more light fragments and fewer heavier fragments are produced in reactions on a heavy target like ^{181}Ta. We found no difference between the mean N_f/Z_f ratios of the isotopes produced on both targets, but there existed an enhancement for the neutron-rich and proton-rich products if the ^{181}Ta target was used. We think that the enhancement for the proton-rich fragments is mostly due to the deexcitation of the prefragments, but for the neutron-rich fragments, the enhancement is dominated by the nucleon-transfer process. However, the discussions are still qualitative, and further investigations are of great interest.

ACKNOWLEDGMENTS

The authors wish to thank the HIRFL staff and crew for their cooperation. This work is supported by the NSFC under Grants No. 10775159, No. 10925526, and No. 11079044, and by the Major State Basic Research Development Program of China under Contract No. G2007CB815000.

---

[1] I. Tanihata, D. Hirata, T. Kobayashi, S. Shimoura, K. Sugimoto, and H. Toki, Phys. Lett. B **289**, 261 (1992).

[2] N. Fukunishi, T. Otsuka, and I. Tanihata, Phys. Rev. C **48**, 1648 (1993).

[3] T. Motobayashi, Y. Ikeda, K. Ieki, M. Inoue, N. Iwasa, T. Kikuchi, M. Kurokawa, S. Moriya, S. Ogawa, H. Murakami, S. Shimoura, Y. Yanagisawa, T. Nakamura, Y. Watanabe, M. Ishihara, T. Teranishi, H. Okuno, and R. F. Casten, Phys. Lett. B **346**, 9 (1995).

[4] R. Anne, D. Bazin, A. C. Mueller, J. C. Jacmart, and M. Langevin, Nucl. Inst. Meth A **257**, 215 (1987).

[5] B. M. Sherrill, D. J. Morrissey, J. A. Nolen Jr., and J. A. Winger, Nucl. Inst. Meth. B **56/57**, 1106 (1991).

[6] T. Kubo, M. Ishihara, N. Inabe, H. Kumagai, I. Tanihata, K. Yoshida, T. Nakamura, H. Okuno, S. Shimoura, and K. Asahi, Nucl. Inst. Meth. B **70**, 309 (1992).

[7] H. Geissel, P. Armbruster, K. H. Behr, A. Brünle, K. Burkard, M. Chen, H. Folger, B. Franczak, H. Keller, O. Klepper, B. Langenbeck, F. Nickel, E. Pfeng, M. Pfützner, E. Roeckl, K. Rykaczewski, I. Schall, D. Schardt, C. Scheidenberger, K.-H. Schmidt, A. Schröter, T. Schwab, K. Sümmerer, M. Weber, G. Münzenberg, T. Brohm, H.-G. Clerc, M. Fauerbach, J.-J. Gaimard, A. Grewe, E. Hanelt, B. Knödler, M. Steiner, B. Voss, J. Weckenmann, C. Ziegler, A. Magel, H. Wollnik, J. P. Dufour, Y. Fujita, D. J. Vieira, and B. Sherrill, Nucl. Inst. Meth. B **70**, 286 (1992).

[8] H. H. Heckman, D. E. Greiner, P. J. Lindstrom, and F. S. Bisser, Science **174**, 1130 (1971).

[9] H. A. Grunder, W. D. Hartsough, and E. J. Lofgren, Science **174**, 1128 (1971).

[10] D. E. Greiner, P. J. Lindstrom, H. H. Heckman, Bruce Cork, and F. S. Bieser, Phys. Rev. Lett. **35**, 152 (1975).

[11] V. Borrel, B. Gatty, D. Guerreau, J. Galin, and D. Jacquet, Z. Phys. A **324**, 205 (1986).

[12] A. S. Goldhaber, Phys. Lett. B **53**, 306 (1974).

[13] K. Sümmerer and B. Blank, Phys. Rev. C **61**, 034607 (2000).

[14] J. D. Bowman, W. J. Swiatecki, and C. F. Tsang, LBL Report LBL-2908 (1973).

[15] D. L. Olson, B. L. Berman, D. E. Greiner, H. H. Heckman, P. J. Lindstrom, and H. J. Crawford, Phys. Rev. C **28**, 1602 (1983).

[16] J. R. Cummings, W. R. Binns, T. L. Garrard, M. H. Israel, J. Klarmann, E. C. Stone, and C. J. Waddington, Phys. Rev. C **42**, 2530 (1990).

[17] M. C. Mermaz, V. Borrel, D. Guerreau, J. Galin, B. Gatty, and D. Jacquet, Z. Phys. A **324**, 217 (1986).

[18] M. Mocko, M. B. Tsang, L. Andronenko, M. Andronenko, F. Delaunay, M. Famiano, T. Ginter, V. Henzl, D. Henzlová, H. Hua, S. Lukyanov, W. G. Lynch, A. M. Rogers, M. Steiner, A. Stolz, O. Tarasov, M.-J. van Goethem, G. Verde, W. S. Wallace, and A. Zalessov, Phys. Rev. C **74**, 054612 (2006).

[19] M. Mocko, M. B. Tsang, Z. Y. Sun, N. Aoi, J. M. Cook, F. Delaunay, M. A. Famiano, H. Hui, N. Imai, H. Iwasaki, W. G. Lynch, T. Motobayashi, M. Niikura, T. Onishi, A. M. Rogers, H. Sakurai, A. Stolz, H. Suzuki, E. Takeshita, S. Takeuchi, and M. S. Wallace, Phys. Rev. C **76**, 014609 (2007).

[20] M. Notani, H. Sakurai, N. Aoi, H. Iwasaki, N. Fukuda, Z. Liu, K. Yoneda, H. Ogawa, T. Teranishi, T. Nakamura, H. Okuno, A. Yoshida, Y. X. Watanabe, S. Momota, N. Inabe, T. Kubo, S. Ito, A. Ozawa, T. Suzuki, I. Tanihata, and M. Ishihara, Phys. Rev. C **76**, 044605 (2007).

[21] M. Mocko, M. B. Tsang, D. Lacroix, A. Ono, P. Danielewicz, W. G. Lynch, and R. J. Charity, Phys. Rev. C **78**, 024612 (2008).

[22] J. W. Xia, Y. F. Wang, Y. N. Rao, Y. J. Yuan, M. T. Song, W. Z. Zhang, P. Yuan, W. Gu, X. T. Yang, X. D. Yang, S. L. Lin, H. W. Zhao, J. Y. Tang, W. L. Zhan, B. W. Wei, Y. Yano, A. Goto, T. Katayama, and S. Watanabe, *Proceedings of the First Asian Particle Accelerators Conference*, KEK, Japan (1998), p. 342.

[23] J. W. Xia, W. L. Zhan, B. W. Wei, Y. J. Yuan, M. T. Song, W. Z. Zhang, X. D. Yang, P. Yuan, D. Q. Gao, H. W. Zhao, X. T. Yang, G. Q. Xiao, K. T. Man, J. R. Dang, X. H. Cai, Y. F. Wang, J. Y. Tang, W. M. Qiao, Y. N. Rao, Y. He, L. Z. Mao, and Z. Z. Zhou, Nucl. Inst. Meth. A **488**, 11 (2002).

[24] Z. Sun, W.-L. Zhan, Z.-Y. Guo, G. Xiao, and J.-X. Li, Nucl. Inst. Meth. A **503**, 496 (2003).

[25] C. Ziegler, T. Brohm, H. G. Clerc, H. Geissel, K. H. Schmidt, K. Summerer, D. Vieira, and B. Voss, Sci. Rep. GSI **1**, 291 (1991).

[26] Y. X. Zhao, W. L. Zhan, Z. Y. Guo, H. F. Xi, J. Q. Zhou, H. H. Lei, J. C. Wang, Y. F. Luo, E. P. Feng. Nucl, Inst. Meth. A **355**, 464 (1995).

[27] D. Bazin, O. Tarasov, M. Lewitowicz, and O. Sorlin, Nucl. Inst. Meth. A **482**, 307 (2002).

[28] O. Tarasov, Nucl. Phys. A **734**, 536 (2004).

[29] K. V. Bibber, D. L. Hendrie, D. K. Scott, H. H. Weiman, L. S. Schroeder, J. V. Geaga, S. A. Cessin, R. Treuhaft, Y. J. Grossiord, J. O. Rasmussen, and C. Y. Wong, Phys. Rev. Lett. **43**, 840 (1979).

[30] Y. P. Viyogi, T. J. M. Symons, P. Doll, D. E. Greiner, H. H. Heckman, D. L. Hendrie, P. J. Lindstrom, J. Mahoney, D. K. Scott, K. Van Bibber, G. D. Westfall, and H. Wieman, H. J. Crawford, C. McParland, and C. K. Gelbke, Phys. Rev. Lett. **42**, 33 (1979).

[31] M. Weber, C. Donzaud, J. P. Dufour, H. Geissel, A. Grewe, D. Guillemaud-Mueller, H. Keller, M. Lewitowicz, A. Magel, A. C. Muellerb, G. Münzenberg, F. Nickel, M. Pfützner, A. Piechaczek, M. Pravikoff, E. Roeckl, K. Rykaczewski, M. G. Saint-Laurent, I. Schall, C. Stéphan, K. Sümmerer, L. Tassan-Got, D. J. Vieira, and B. Voss, Nucl. Phys. A **578**, 659 (1994).

[32] M. Caamaño, D. Cortina-Gil, K. Sümmerer, J. Benlliure, E. Casarejos, H. Geissel, G. Münzenberg, and J. Pereira, Nucl. Phys. A **733**, 187 (2004).

[33] V. Borrel, D. Guerreau, J. Galin, B. Gatty, D. Jacquet, and X. Tarrago, Z. Phys. A **314**, 191 (1983).

[34] F. Rami, J. P. Coffin, G. Guillaume, B. Heusch, P. Wagner, A. Fahli, and P. Fintz, Nucl. Phys. A **444**, 325 (1985).

[35] D. Lacroix, A. V. Lauwe, and D. Durand, Phys. Rev. C **69**, 054604 (2004).

[36] G. D. Westfall, J. Gosset, P. J. Johansen, A. M. Poskanzer, W. G. Meyer, H. H. Gutbrod, A. Sandoval, and R. Stock, Phys. Rev. Lett. **37**, 1202 (1976).

[37] O. B. Tarasov and D. Bazin, Nucl. Inst. Meth. B **266**, 4657 (2008).

[38] J. J. Gaimard and K. H. Schmidt, Nucl. Phys. A **531**, 709 (1991).

[39] O. B. Tarasov and D. Bazin, Nucl. Inst. Meth. B **204**, 174 (2003).

[40] [http://caeinfo.in2p3.fr/theorie/hipse.htm].

[41] D. Durand, Nucl. Phys. A **541**, 266 (1992).

[42] E. Kwan, Ph.D. thesis, Michigan State University 2006 (unpublished).

[43] D. Guerreau, Nucl. Phys. A **447**, 37 (1985).

[44] K. H. Schmidt, M. V. Ricciardi, A. S. Botvina, and T. Enqvist, Nucl. Phys. A **710**, 157 (2002).

[45] G. A. Souliotis, D. V. Shetty, M. Veselsky, G. Chubarian, L. Trache, A. Keksis, and E. Martin, and S. J. Yennello. Phys. Rev. C **68**, 024605 (2003).

[46] M. Geraci, G. Lanzanò, E. D. Filippo, A. Pagano, J. L. Charvet, R. Dayras, R. Legrain, C. Volant, J. Richert, and P. Wagner, Nucl. Phys. A **773**, 1 (2006).

[47] K. Chen, Z. Fraenkel, G. Friedlander, J. R. Grover, J. M. Miller, and Y. Shimamoto, Phys. Rev. **166**, 949 (1968).